Determination of Land and Ocean Reflective, Radiative, and Biophysical Properties Using Multiangle Imaging

John V. Martonchik, David J. Diner, Bernard Pinty, Michel M. Verstraete, *Member, IEEE*, Ranga B. Myneni, Yuri Knyazikhin, and Howard R. Gordon

***Abstract*— Knowledge of the directional and hemispherical reflectance properties of natural surfaces, such as soils and vegetation canopies, is essential for classification studies and canopy model inversion. The Multi-angle Imaging SpectroRadiometer (MISR), an instrument to be launched in 1998 onboard the EOS-AM1 platform, will make global observations of the earth's surface at 1.1-km spatial resolution, with the objective of determining the atmospherically corrected reflectance properties of most of the land surface and the tropical ocean. The algorithms to retrieve surface directional reflectances, albedos, and selected biophysical parameters using MISR data are described. Since part of the MISR data analyses includes an aerosol retrieval, it is assumed that the optical properties of the atmosphere (i.e., aerosol characteristics) have been determined well enough to accurately model the radiative transfer process. The core surface retrieval algorithms are tested on simulated MISR data, computed using realistic surface reflectance and aerosol models, and the sensitivity of the retrieved directional and hemispherical reflectances to aerosol type and column amount is illustrated. Included is a summary list of the MISR surface products.**

***Index Terms*— Algorithms, reflection, remote sensing, vegetation.**

I. Introduction

ABOUT 30% of the Earth's surface is covered by land and much of this is vegetated. Thus, land surface processes are important components of the terrestrial climate system [1]. The bulk of the solar energy provided to the troposphere transits through to the lower boundary (oceans and continents) first and is made available to the atmosphere through the fluxes of sensible and latent heat and thermal radiation. Accurate descriptions of the interaction of surface vegetation and atmospheric processes require quantitative information on fluxes of energy (radiation) and mass (water vapor and CO_2), which are strong functions of photosynthetic and evapotranspiration rates. These, in turn, are strongly correlated with surface hemispherical reflectance (i.e., albedo) [2]–[4]. Therefore, accurate hemispherical reflectance estimates are expected to be diagnostic of the influence of biophysical processes on surface-atmosphere interactions. These estimates are also important, even over nonvegetated terrain, because modifications to the surface, through natural or human-induced causes, will potentially change the hemispherical reflectance and, consequently, impact the climate system as a result of perturbing the lower boundary condition [5]–[7].

Angular signature information is also expected to be a significant component of improved surface cover classification and characterization [8]. The time-evolution of terrestrial ecosystems is difficult to monitor at the surface, and satellite platforms provide a unique opportunity to carry out extensive surveys with comprehensive spatial coverage and high time resolution. Detection of ecophysiological change on the land surface, resulting from natural processes (canopy succession and species replacement) or anthropogenic activities (e.g., deforestation, acid rain), necessitates accurate, repeatable measurements of the surface that can be used for landscape classification. Over oceans, monitoring of ocean color provides the means of monitoring marine biological productivity and its changes with time.

In an effort to meet these observational needs, the Multiangle Imaging SpectroRadiometer (MISR), scheduled for launch in 1998 on the EOS-AM1 platform, is capable of continuously imaging the earth's surface at nine fixed viewing angles (70.5, 60.0, 45.6, and 26.1° forward and aftward of nadir and nadir) and four spectral bands (446, 558, 672, and 866 nm) [9]. Thus, a given scene will be observed at these viewing angles and wavelengths within a span of only 7 min, i.e., near simultaneously, allowing the assumption that the cloud-free atmosphere over the scene remains constant during the course of the measurements. The MISR surface retrievals will be performed at the spatial resolution of 1.1 km globally, termed a subregion, but localized areas of interest can be processed at MISR's highest resolution of 275 m.

II. Surface Retrieval Strategy

Before surface retrievals can be performed within a given region, various atmospheric parameters need to be determined by means of an aerosol retrieval. Here, a region is defined to be

Manuscript received November 3, 1997; revised February 21, 1998. This work was supported by the Jet Propulsion Laboratory, California Institute of Technology, under contract with the National Aeronautics and Space Administration.

J. V. Martonchik and D. J. Diner are with the Jet Propulsion Laboratory, California Institute of Technology, Pasadena, CA 91109 USA (e-mail: jvm@jord.jpl.nasa.gov).

B. Pinty and M. M. Verstraete are with the Space Applications Institute, EC Joint Research Centre, I-21020 Ispra (VA), Italy.

R. B. Myneni and Y. Knyazikhin are with the Department of Geography, Boston University, Boston, MA 02215 USA.

H. R. Gordon is with the Department of Physics, University of Miami, Coral Gables, FL 33124 USA.

Publisher Item Identifier S 0196-2892(98)04166-7.

an area 17.6 × 17.6 km in size, composed of 16 × 16 1.1-km subregions, covering either land or ocean. However, an aerosol retrieval is not performed if the region exhibits too much cloudiness or if the surface terrain is too topographically complex. Even if an aerosol retrieval was successful, some 1.1-km subregions within the region may not be suitable for a surface retrieval, due to cloudiness, cloud shadows, sun glitter (usually over water), or instrument-related reasons.

The following sequence of land surface retrieval activity is performed on all suitable subregions. First, the hemispherical-directional reflectance factor (HDRF) for all available camera view angles and the bihemispherical reflectance (BHR) are determined in the four MISR spectral bands. The HDRF at a surface location (x, y) is defined as the ratio of the view-angle-dependent surface-reflected radiance at (x, y) to the reflected radiance from an ideal (i.e., unit albedo) Lambertian target for the same incident radiance field as that at (x, y). Therefore, since the radiance from a Lambertian surface is proportional to the irradiance, the HDRF can be considered to be the surface-leaving radiance, scaled by a known irradiance. The BHR, an albedo, is defined as the ratio of the exiting surface flux (radiant exitance) to the incident surface flux (irradiance) and is proportional to the HDRF, integrated over the view angle hemisphere. It is important to note that the HDRF and its BHR are obtained under the illumination conditions of the ambient atmosphere (i.e., direct and diffuse sunlight) and are retrieved from the MISR observations with a minimum number of assumptions. Since these parameters are directly related to radiances and fluxes at the surface, they provide information to radiation balance studies of the atmosphere/surface system. Using the HDRF as a starting point, the associated bidirectional reflectance factor (BRF) and the directional-hemispherical reflectance (DHR) are determined. The BRF and the DHR are equivalent surface properties to the HDRF and BHR, respectively, but are defined for unattenuated direct sunlight illumination only (i.e., in the absence of an atmosphere). It is straightforward to obtain the BRF from the HDRF by removing the effects of the diffuse sunlight and the attenuated direct sunlight, but diffuse sunlight effects can be removed only if a BRF model is assumed. As a consequence, the BRF and DHR are somewhat more model dependent than the HDRF and the BHR. By using a parameterized BRF model, however, and determining the model parameters, the possibility exists of extrapolating the retrieved BRF and DHR to other view and sun angles not obtainable by MISR.

From the spectral BHR and DHR, a photosynthetically active radiation (PAR)-integrated BHR and DHR are obtained. The PAR band covers the 400–700-nm wavelength range. The PAR-integrated BHR and DHR are a measure of the amount of PAR absorbed by the surface (vegetative and nonvegetative) under ambient and direct illumination conditions, respectively. The fractional amount of incident PAR absorbed by vegetation canopies (FPAR) only (and not the understory or soil) and the canopy leaf area index (LAI) are then estimated using the retrieved spectral surface products (BHR, DHR, BRF, HDRF) as input to detailed radiative transfer models of various plant canopy biome types. The details of the LAI/FPAR algorithm can be found in [10].

The ocean surface retrieval process is performed only for the tropical ocean, which for our purpose is contained within a 600-km wide band centered on the equator. Phytoplankton pigment concentration is estimated by using the retrieved water-leaving radiances in the MISR blue (446 nm) and green (558 nm) bands as input to a modified Coastal Zone Color Scanner (CZCS) algorithm. However, these water-leaving radiances are retrieved in two distinct ways. One is the conventional approach, essentially employing the Moderate Resolution Imaging Spectroradiometer (MODIS)/SeaWiFS algorithm [11], [12], which has its own collection of aerosol models, and the other is based on the MISR aerosol and HDRF retrieval algorithms. Pigment concentrations are determined using both sets of water-leaving radiances for later comparison studies.

III. Surface Retrieval Preliminaries

The algorithms assume that scattering and absorption of sunlight within the atmosphere is adequately described by radiative transfer theory [13]. In general, attenuation of the incident and reflected beams as a result of extinction (scattering and absorption) along the ray path is somewhat offset by diffuse radiation that has been 1) reflected by the atmosphere without reaching the surface, 2) subjected to multiple reflections between the atmosphere and surface, and 3) scattered into the line-of-sight from neighboring areas. The top-of-atmosphere (TOA) radiance depends on both the optical characteristics of the atmosphere and the reflectance properties (spatial, spectral, and angular) of the surface. The solution to the radiative transfer equation is an integral expression that must be solved for the surface reflectance. At the bottom of the atmosphere, the surface is illuminated by radiation that has been both directly and diffusely transmitted through the atmosphere as well as by backscattered light from the surface. The diffuse radiation field, called skylight, illuminates the surface from all angles in the downward hemisphere. In contrast, directly transmitted sunlight is more or less unidirectional (except for the finite angular size of the sun, which can be ignored for practical purposes).

An implicit assumption of the surface retrieval algorithms is that each of the 36 (9 view angles × 4 spectral bands) MISR radiances is associated with the same ground footprint, particularly with regard to size. At the highest resolution, the geometric cross-track footprint dimension of each camera is virtually the same, about 275 m, as a consequence of the particular camera effective focal length. However, surface projection effects increase the geometric along-track footprint dimension with increasing view angle. Thus, the along-track instantaneous footprint size of the D (70.5°) cameras at the highest resolution is three times that of the off-nadir A (26.1°) cameras, 707 m versus 236 m, but the along-track sample spacing is still 275 m. When the high-resolution samples are averaged 4 × 4 to create a subregion with a cross-track dimension of 1.1 km, the surface projection effect is substantially mitigated for the subregion along-track dimension, due to the 275-m sample spacing. Thus, subregions from the D, C (60.0°) and B (45.6°) cameras are only 17, 11, and 6% geometrically larger, respectively, than subregions

from the A cameras. These variations in footprint size are not considered significant, and so the common subregions from all nine cameras are treated in the retrieval process as having identical ground footprints.

Because the surface topography is variable within the footprints of the MISR observations, the effects of terrain slope must be considered in the surface retrieval. The primary effects of a sloped or tilted terrain on the observed radiance include the dependence of irradiance (both direct and diffuse), upward transmittance, and possibly surface BRF on the tilt angle (slope). Some of these effects have been studied insofar as how they impact the classification accuracy of forest canopies (e.g., [14] and [15]). A more general analysis was done by Woodham and Lee [16], who devised a six-parameter model of surface reflectance to account for slope effects. Using this model, Gray [17] reported that the classification accuracy for a forested area increased from 51% [uncorrected Landsat Multi-Spectral Scanner (MSS) data] to 80% with correction for the solar incidence angle providing the largest effect. If, however, the slope is kept under 20°, the atmospheric parameters associated with diffuse scattering seem to depend only slightly on the slope angle [15]. Therefore, surface parameters will be retrieved only for subregions with slopes within the 20° limit by using a topographic mask to filter out more rugged terrain. In this case, the MISR surface retrievals do not need to explicitly incorporate tilt or slope effects. Instead, in every 1.1-km land subregion where a retrieval is performed, the surface-leaving radiance is considered to transition an imaginary horizontal surface (a surface parallel to the standard earth ellipsoid) and the MISR surface retrieval results are referenced to this surface. Certain mountainous regions obviously will be excluded from standard product generation activities, but it is expected that they will be investigated on a specialized basis.

Although the adjacency effect is also mentioned in the above cited references, there are few operational methods to correct for reflections from adjacent, spatially heterogeneous terrain, especially at off-nadir view angles (see [18]). For spacecraft measurements, these adjacency effects can be described by a convolution of the three-dimensional (3-D) upward transmittance and the surface-leaving radiance. The radiance $L^{TOA}_{\lambda,x,y'}$, leaving the top of the atmosphere at wavelength λ when viewing the surface at spatial coordinates x, y, can be written as

$$\begin{aligned} L^{TOA}_{\lambda,x,y}&(-\mu,\,\mu_0,\,\phi-\phi_0;\,\tau_\lambda) \\ &= L^{atm}_{\lambda}(-\mu,\,\mu_0,\,\phi-\phi_0;\,\tau_\lambda) \\ &\quad + e^{-\tau_\lambda/\mu}\cdot L^{surf}_{\lambda,x,y}(-\mu,\,\mu_0,\,\phi-\phi_0;\,\tau_\lambda) \\ &\quad + \int_0^1\int_0^{2\pi} T_{\lambda,x,y}(-\mu,\,-\mu',\phi-\phi';\,\tau_\lambda) \\ &\quad \otimes L^{surf}_{\lambda,x,y}(-\mu',\,\mu_0,\,\phi'-\phi_0;\,\tau_\lambda)\,d\mu'\,d\phi' \end{aligned} \tag{1}$$

with

$$\begin{aligned} L^{surf}_{\lambda,x,y}&(-\mu,\,\mu_0,\,\phi-\phi_0;\tau_\lambda) \\ &= \frac{1}{\pi}\int_0^1\int_0^{2\pi} R_{\lambda,x,y}(-\mu,\,\mu',\,\phi-\phi') \\ &\quad \cdot L^{inc}_{\lambda,x,y}(\mu',\,\mu_0,\,\phi'-\phi_0;\,\tau_\lambda)\mu'\,d\mu'\,d\phi'. \end{aligned} \tag{2}$$

Here, μ and μ_0 are the cosines of the view and sun angles, defined with respect to the normal to the surface ellipsoid (not the local topographically defined surface orientation) and $\phi-\phi_0$ is the view azimuthal angle, with respect to the sun position, also in the ellipsoid reference system. The convention $-\mu$ and μ is used for upwelling and downwelling radiation, respectively. The properties of the atmosphere are assumed to be horizontally homogeneous within the volume defined by the measurements. In (1), L^{atm}_{λ} is the radiance scattered by the atmosphere to space without interacting with the surface (i.e., the path radiance), $L^{surf}_{\lambda,x,y}$ is the surface-leaving radiance, $T_{\lambda,x,y}$ is the upward diffuse transmittance, and τ_λ is the optical depth of the atmosphere (Rayleigh + aerosols). In (2), $L^{inc}_{\lambda,x,y}$ is the direct and diffuse downward radiance incident on the surface, and $R_{\lambda,x,y}$ is the surface BRF. The BRF is π times the bidirectional reflectance distribution function (BRDF).

In the general 3-D solution to the radiative transfer problem with a horizontally uniform atmosphere over a spatially flat but contrasting surface, the transmittance $T_{\lambda,x,y}$ can be thought of as a point-spread function and the convolution operation $\otimes$ describes the blurring effect of the atmosphere on the surface reflectance $R_{\lambda,x,y}$ [19]. When the image spatial resolution is comparable to or greater than the atmospheric scattering scale height (defined by the vertical distribution of the aerosols and/or Rayleigh scattering molecules), adjacency effects are mitigated and (1) reduces to the standard one-dimensional (1-D) radiative transfer regime, where $T_{\lambda,x,y}$ is effectively a delta function in the spatial coordinates. In this case, (1) simplifies to

$$\begin{aligned} L^{TOA}_{\lambda,x,y}&(-\mu,\,\mu_0,\,\phi-\phi_0;\,\tau_\lambda) \\ &= L^{atm}_{\lambda}(-\mu,\,\mu_0,\,\phi-\phi_0;\,\tau_\lambda) \\ &\quad + e^{-\tau_\lambda/\mu}\cdot L^{surf}_{\lambda,x,y}(-\mu,\,\mu_0,\,\phi-\phi_0;\,\tau_\lambda) \\ &\quad + \int_0^1\int_0^{2\pi} T_{\lambda}(-\mu,\,-\mu',\,\phi-\phi';\,\tau_\lambda) \\ &\quad \cdot L^{surf}_{\lambda,x,y}(-\mu',\,\mu_0,\,\phi'-\phi_0;\,\tau_\lambda)\,d\mu'\,d\phi'. \end{aligned} \tag{3}$$

Over oceans, the 1-D radiative transfer description of the TOA radiance, described by (3), is appropriate, due mainly to a lack of contrast on the ocean surface. Over land, however, there can be significant surface contrast and aerosol scale heights are about 1–2 km, comparable to the surface spatial resolution, leading to adjacency effects. Nevertheless, by virtue of the 1.1-km subregion size, we assume that (3) is sufficiently accurate, such that surface retrievals are not significantly compromised by not using (1). This assumption has been tested using a 3-D radiative transfer algorithm [20], [21] on a scene with a high-contrast boundary (a coastline) [22]. The results of these tests indicate that at the spatial resolution corresponding to unaveraged MISR data (275 m) and especially at high spatial resolution (30 m or finer) obtained with sensors, such as the Landsat Thematic Mapper, SPOT, or ASTER, the use of (3) can lead to retrieved surface reflectances with errors larger than those resulting from expected uncertainties in the aerosol retrieval. At the 1.1-km subregion size, however, the errors resulting from the use of 1-D radiative transfer theory are similar in magnitude to errors incurred with the

aerosol retrieval. Therefore, until we are confident that aerosol retrieval errors can be minimized, we do not consider the additional complexities of including 3-D radiative transfer theory to be warranted.

Finally, a principal assumption in the surface retrieval process is that the state of the atmosphere is known well enough that the various atmosphere-dependent functions, e.g., T_λ and L_λ^{atm} in (3), can be determined. For MISR, this process involves an aerosol retrieval [23] that allows a determination of the atmospheric optical depth (aerosol + Rayleigh) and its scattering properties (phase function and single scattering albedo) in the four MISR spectral bands. This information is then used as input to lookup tables of radiative transfer parameters contained in the Simulated MISR Ancillary Radiative Transfer (SMART) data set [24]. The use of the SMART data set is an efficient alternative to real-time computations of parameters, such as atmospheric path radiance, diffuse transmittance, and irradiance. This data set is used in the aerosol retrieval process, and it provides the necessary atmospheric quantities in (3), needed by the surface retrieval algorithms.

IV. Retrieval of HDRF and BHR

The retrieved HDRF is essentially a measure of surface-leaving radiance at the nine MISR view angles and four spectral bands for the particular sun angle geometry of the observations. Integration of the HDRF over the sky hemisphere results in the BHR or surface albedo for ambient sky illumination. These kinds of data currently are being obtained for very localized areas as part of sporadically timed field experiments by using hand-held radiometers with footprint sizes of less than a meter (see [25]). In contrast, MISR will provide the HDRF and BHR systematically with a footprint size of 1.1 km over most of the global land surface. The retrieval algorithm described below simultaneously retrieves the spectral HDRF and BHR.

The description of the HDRF/BHR retrieval algorithm begins with a mathematical definition of the *HDRF for nonisotropic incident radiation*, the full descriptor of the HDRF. It can be written as

$$r_{\lambda,x,y}(-\mu,\mu_0,\phi-\phi_0;\tau_\lambda) = \frac{L^{surf}_{\lambda,x,y}(-\mu,\mu_0,\phi-\phi_0;\tau_\lambda)}{\frac{1}{\pi}\int_0^1\int_0^{2\pi} L^{inc}_{x,y}(\mu',\mu_0,\phi'-\phi_0;\tau_\lambda)\mu'\,d\mu'\,d\phi'} \quad (4)$$

and is equal to the ratio of the radiance reflected from the surface $L^{surf}_{\lambda,x,y}$ to the radiance reflected from an ideal Lambertian target, each with the same beam geometry and illuminated under identical atmospheric conditions. The surface irradiance $E_{\lambda,x,y}$ is defined as

$$E_{\lambda,x,y}(\mu_0;\tau_\lambda) = \int_0^1\int_0^{2\pi} L^{inc}_{\lambda,x,y}(\mu',\mu_0,\phi'-\phi_0;\tau_\lambda)\cdot\mu'\,d\mu'\,d\phi' \quad (5)$$

and is the incident flux (or, more precisely, the radiant flux density) at the surface. The total radiance incident on the surface $L^{inc}_{\lambda,x,y}$ in (5) includes the contribution from all of the multiple reflections between the atmosphere and surface and, therefore, $E_{\lambda,x,y}$ is dependent on the surface BRF $R_{\lambda,x,y}$.

Another basic radiometric quantity is the radiant exitance at the surface $M_{\lambda,x,y}$, expressed as

$$M_{\lambda,x,y}(\mu_0;\tau_\lambda) = \int_0^1\int_0^{2\pi} L^{surf}_{\lambda,x,y}(-\mu,\mu_0,\phi-\phi_0;\tau_\lambda)\cdot\mu\,d\mu\,d\phi \quad (6)$$

and is the exiting radiant flux density at the surface.

Now, when $r_{\lambda,x,y}$ in (4) is integrated over the hemisphere, the result $A^{hem}_{\lambda,x,y}$ is the *BHR for nonisotropic incident radiation*, i.e.,

$$\begin{aligned} A^{hem}_{\lambda,x,y}(\mu_0;\tau_\lambda) &= \frac{1}{\pi}\int_0^1\int_0^{2\pi} r_{\lambda,x,y}(-\mu,\mu_0,\phi-\phi_0;\tau_\lambda)\cdot\mu\,d\mu\,d\phi \\ &= \frac{M_{\lambda,x,y}(\mu_0;\tau_\lambda)}{E_{\lambda,x,y}(\mu_0;\tau_\lambda)}. \end{aligned} \quad (7)$$

Thus, the BHR is the ratio of the radiant exitance to the irradiance, i.e., the albedo.

The surface-dependent irradiance $E_{\lambda,x,y}$ is related to the black surface irradiance $E_{\lambda,b}$ via the highly accurate approximation (exact for a Lambertian reflecting surface)

$$E_{\lambda,x,y}(\mu_0;\tau_\lambda) = \frac{E_{\lambda,b}(\mu_0;\tau_\lambda)}{1-A^{hem}_{\lambda,x,y}(\mu_0;\tau_\lambda)\cdot s_\lambda(\tau_\lambda)} \quad (8)$$

where s_λ is the bottom-of-atmosphere (BOA) bihemispherical albedo. This expression for $E_{\lambda,x,y}$ quantifies the effect of the multiple bounces of radiation between the surface and the atmosphere. Combining (7) and (8), the expression for $A^{hem}_{\lambda,x,y}$ can then be rewritten as

$$A^{hem}_{\lambda,x,y}(\mu_0;\tau_\lambda) = \frac{M_{\lambda,x,y}(\mu_0;\tau_\lambda)}{E_{\lambda,b}(\mu_0;\tau_\lambda)+s_\lambda(\tau_\lambda)\cdot M_{\lambda,x,y}(\mu_0;\tau_\lambda)}. \quad (9)$$

Also, using (5) and (8), $r_{\lambda,x,y}$ can be rewritten as in (10), shown at the bottom of the page. Thus, when $L^{surf}_{\lambda,x,y}$ is known, $r_{\lambda,x,y}$ and $A^{hem}_{\lambda,x,y}$ can be computed from (6), (9), and (10). The other parameters in these equations, the black surface irradiance $E_{\lambda,b}$, the BOA bihemispherical albedo s_λ, and the atmospheric optical depth τ_λ, depend only on atmospheric properties and are determined in the aerosol retrieval process.

$$r_{\lambda,x,y}(-\mu,\mu_0,\phi-\phi_0;\tau_\lambda) = \frac{\pi\cdot L^{surf}_{\lambda,x,y}(-\mu,\mu_0,\phi-\phi_0;\tau_\lambda)\cdot\left[1-A^{hem}_{\lambda,x,y}(\mu_0;\tau_\lambda)\cdot s_\lambda(\tau_\lambda)\right]}{E_{\lambda,b}(\mu_0;\tau_\lambda)} \quad (10)$$

The integral equation (3) can be solved for $L^{surf}_{\lambda,x,y}$ by starting with an initial estimate and converging to the solution via iteration. An initial estimate $L^{surf(0)}_{\lambda,x,y}$ is made by using (3), but with $L^{surf}_{\lambda,x,y}$ in the diffuse transmittance term brought outside the integral. Then, we can write

$$L^{surf(0)}_{\lambda,x,y}(-\mu,\mu_0,\phi-\phi_0;\tau_\lambda) = \frac{L^{\mathrm{MISR}}_{\lambda,x,y}(-\mu,\mu_0,\phi-\phi_0) - L^{atm}_{\lambda}(-\mu,\mu_0,\phi-\phi_0;\tau_\lambda)}{e^{-\tau_\lambda/\mu}+t_\lambda(-\mu;\tau_\lambda)} \tag{11}$$

where

$$t_\lambda(-\mu;\tau_\lambda) = \int_0^1\int_0^{2\pi} T_\lambda(-\mu,-\mu',\phi-\phi';\tau_\lambda)\,d\mu'\,d\phi' \tag{12}$$

and $L^{\mathrm{MISR}}_{\lambda,x,y}$ is identified with the TOA radiance $L^{TOA}_{\lambda,x,y}$. The iteration algorithm for $L^{surf}_{\lambda,x,y}$ is also derived from (3)

$$\begin{aligned} L^{surf(n+1)}_{\lambda,x,y}&(-\mu,\mu_0,\phi-\phi_0;\tau_\lambda) \\ &= \left[L^{MISR}_{\lambda,x,y}(-\mu,\mu_0,\phi-\phi_0) - L^{atm}_{\lambda}(-\mu,\mu_0,\phi-\phi_0;\tau_\lambda)\right]\cdot e^{\tau_\lambda/\mu} \\ &\quad - \left[\int_0^1\int_0^{2\pi} T_\lambda(-\mu,-\mu',\phi-\phi';\tau_\lambda) \cdot L^{surf(n)}_{\lambda,x,y}(-\mu',\mu_0,\phi'-\phi_0;\tau_\lambda)\,d\mu'\,d\phi'\right] \\ &\quad \cdot e^{\tau_\lambda/\mu}. \end{aligned} \tag{13}$$

Note that (13) implies that $L^{surf}_{\lambda,x,y}$ is directly determined only at the nine sun-view angles of the MISR observations, but evaluation of the last term requires that $L^{surf}_{\lambda,x,y}$ be known over a complete hemisphere. However, we can obtain a good approximation of this integral if both T_λ and $L^{surf(n)}_{\lambda,x,y}$ are described by a two-term cosine series in azimuth angle. Then, (13) can be rewritten as

$$\begin{aligned} L^{surf(n+1)}_{\lambda,x,y}&(-\mu,\mu_0,\phi-\phi_0;\tau_\lambda) \\ &= \left[L^{MISR}_{\lambda,x,y}(-\mu,\mu_0,\phi-\phi_0) - L^{atm}_{\lambda}(-\mu,\mu_0,\phi-\phi_0;\tau_\lambda)\right]\cdot e^{\tau_\lambda/\mu} - 2\pi\cdot e^{\tau_\lambda/\mu}\int_0^1 T_{\lambda,0}(-\mu,-\mu';\tau_\lambda) \\ &\quad \cdot L^{surf(n)}_{\lambda,0,x,y}(-\mu',\mu_0;\tau_\lambda)\,d\mu' - \pi\cos(\phi-\phi_0) \\ &\quad \cdot e^{\tau_\lambda/\mu}\int_0^1 T_{\lambda,1}(-\mu,-\mu';\tau_\lambda)L^{surf(n)}_{\lambda,0,x,y}(-\mu',\mu_0;\tau_\lambda)\,d\mu' \end{aligned} \tag{14}$$

where

$$\begin{aligned} L^{surf(n)}_{\lambda,x,y}&(-\mu,\mu_0,\phi-\phi_0;\tau_\lambda) \\ &= L^{surf(n)}_{\lambda,0,x,y}(-\mu,\mu_0;\tau_\lambda) + L^{surf(n)}_{\lambda,1,x,y}(-\mu,\mu_0;\tau_\lambda)\cdot\cos(\phi-\phi_0) \end{aligned} \tag{15}$$

$$\begin{aligned} T_\lambda&(-\mu,-\mu_0,\phi-\phi_0;\tau_\lambda) \\ &= T_{\lambda,0}(-\mu,-\mu_0;\tau_\lambda) + T_{\lambda,1}(-\mu,-\mu_0;\tau_\lambda)\cdot\cos(\phi-\phi_0). \end{aligned} \tag{16}$$

$L^{surf(n)}_{\lambda,x,y}$ and $L^{surf(n)}_{\lambda,1,x,y}$ are described by (17) and (18), shown at the bottom of the page, where ϕ_f and ϕ_a are the forward and aftward view azimuth angles of each symmetrically viewing camera pair. Thus, $L^{surf(n)}_{\lambda,0,x,y}$ and $L^{surf(n)}_{\lambda,1,x,y}$ can be calculated for the five unique MISR view zenith angles (70.5, 60.0, 45.6, 26.1, and 0°). To perform the integrations in (14), these quantities are then interpolated to the Radau quadrature points, at which $T_{\lambda,0}$ and $T_{\lambda,1}$ are evaluated. These transmittance coefficients are another product of the aerosol retrieval process, and precomputed values are contained in the SMART data set.

At every iteration step, the BHR $A^{hem(n)}_{\lambda,x,y}$ is evaluated using (9) with $M_{\lambda,x,y}$ from (6), rewritten as

$$M^{(n)}_{\lambda,x,y}(\mu_0;\tau_\lambda) = 2\pi\int_0^1 L^{surf(n)}_{\lambda,0,x,y}(-\mu,\mu_0;\tau_\lambda)\mu\,d\mu. \tag{19}$$

The iteration process is terminated when the condition

$$\frac{|A^{hem(n)}_{\lambda,x,y}(\mu_0;\tau_\lambda) - A^{hem(n-1)}_{\lambda,x,y}(\mu_0;\tau_\lambda)|}{A^{hem(n)}_{\lambda,x,y}(\mu_0;\tau_\lambda)} \le \varepsilon \tag{20}$$

is satisfied. The configurable parameter ε is set to 0.01.

The procedure described by (14) is very fast and very stable, usually requiring three iterations or less to achieve convergence. Once the iteration is finished, (10) is used to evaluate the HDRF $r_{\lambda,x,y}$.

V. Retrieval of BRF and DHR

The algorithm for retrieving the HDRF and BHR from MISR TOA radiances is virtually independent of any particular kind of surface BRF model and is highly accurate when correct atmospheric information is used. Going a step further, it is then possible to retrieve the BRF and DHR from the HDRF by using a parameterized BRF model. The BRF is actually a limiting form of the HDRF, defined for the special condition of no atmosphere. The same limiting form also applies to the relationship between the BHR and the DHR. This implies that there is no diffuse radiation incident on the surface and only

$$\begin{aligned} L^{surf(n)}_{\lambda,0,x,y}(-\mu,\mu_0;\tau_\lambda) = &\frac{1}{[\cos(\phi_f-\phi_0)-\cos(\phi_a-\phi_0)]} \\ &\cdot\left[L^{surf(n)}_{\lambda,x,y}(-\mu,\mu_0,\phi_a-\phi_0;\tau_\lambda)\cos(\phi_f-\phi_0) - L^{surf(n)}_{\lambda,x,y}(-\mu,\mu_0,\phi_f-\phi_0;\tau_\lambda)\cos(\phi_a-\phi_0)\right] \end{aligned} \tag{17}$$

$$L^{surf(n)}_{\lambda,1,x,y}(-\mu,\mu_0;\tau_\lambda) = \frac{L^{surf(n)}_{\lambda,x,y}(-\mu,\mu_0,\phi_f-\phi_0;\tau_\lambda) - L^{surf(n)}_{\lambda,x,y}(-\mu,\mu_0,\phi_a-\phi_0;\tau_\lambda)}{\cos(\phi_f-\phi_0)-\cos(\phi_a-\phi_0)} \tag{18}$$

the direct radiance from the sun. It is the removal of the effects of the diffuse radiance from the HDRF that requires the use of a BRF model in the BRF/DHR algorithm and ultimately makes the retrieved BRF and DHR somewhat model dependent. The BRF/DHR algorithm also determines the BRF surface model parameters, which allows the model to predict the surface angular reflectance properties fully and, thus, to extend the angular range of the BRF and DHR to also include all solar and view angle geometries not covered by the observations. With further research, it may also be possible to obtain a correlation between the model parameters and surface physical parameters (e.g., LAI and leaf orientation parameters) and surface classification types.

A number of BRF surface models have been proposed in the literature, ranging from those with only two–three parameters (see [27]) to those with ten and more parameters (see [28] and [29]). Devising new and better BRF surface models is an ongoing effort by many researchers, and there is no consensus at the present time as to an optimum BRF model for use with multiangle data. Different researchers may want to use different models, depending on the focus of their investigations. If simple models, containing two or three parameters, are used in the inversion process, the retrieved HDRF at the nine MISR angles, associated with individual orbital swaths, will usually be a sufficient data set upon which to perform BRF retrievals. However, if the more complicated BRF surface models are used, containing more than three parameters, the collection of MISR HDRF's, associated with overlapping swaths from multiple orbits and multiple days, will be required. For the MISR at-launch standard product, we have opted for the former strategy and are using a three-parameter, semiempirical, BRF model.

The retrieval algorithm starts with the relationship between the HDRF $r_{\lambda,x,y}$ and the BRF $R_{\lambda,x,y}$, as in (21), shown at the bottom of the page, where (2), (4), and (5) were used. Here, $r_{\lambda,x,y}$ and $A^{hem}_{\lambda,x,y}$ have been retrieved previously and the irradiance $E_{\lambda,x,y}$ is computed using (8). The incident radiance $L^{inc}_{\lambda,x,y}$ at the surface is approximated by the form

$$\begin{aligned} L^{inc}_{\lambda,x,y}&(\mu,\mu_0,\phi-\phi_0;\tau_\lambda) \\ &\cong E_{0,\lambda}e^{-\tau_\lambda/\mu_0}\cdot\delta(\mu-\mu_0)\cdot\delta(\phi-\phi_0)+E_{0,\lambda} \\ &\quad\cdot\left[\overline{T}_{\lambda,0}(\mu,\mu_0;\tau_\lambda)+\overline{T}_{\lambda,1}(\mu,\mu_0;\tau_\lambda)\cos(\phi-\phi_0)\right] \\ &\quad+\frac{A^{hem}_{\lambda,x,y}(\mu_0;\tau_\lambda)\cdot s_\lambda(\tau_\lambda)}{\pi}\cdot E_{\lambda,x,y}(\mu_0;\tau_\lambda) \end{aligned} \tag{22}$$

where δ is the Dirac delta function and $E_{0,\lambda}$ is the TOA solar irradiance. The downward diffuse transmittance $\overline{T}_\lambda$ is described by a two-term cosine series in $\phi-\phi_0$, where the coefficients $\overline{T}_{\lambda,0}$ and $\overline{T}_{\lambda,1}$ are defined as in (16) for the upward diffuse transmittance. The first term on the right-hand-side of (22) describes the direct radiance, the second term approximates the diffuse downwelling radiance in the absence of any surface reflectance (i.e., a black surface), and the last term approximates the downwelling radiance due to multiple reflections between the atmosphere and the surface.

There is a reciprocity relationship between the upward and downward diffuse transmittances (see [13]), namely

$$\mu\cdot T_\lambda(-\mu,-\mu',\phi-\phi';\tau_\lambda)=\mu'\cdot\overline{T}_\lambda(\mu',\mu,\phi'-\phi;\tau_\lambda). \tag{23}$$

Substituting (22) for $L^{inc}_{\lambda,x,y}$ in (21) and using (16) and (23)

$$\begin{aligned} r_{\lambda,x,y}&(-\mu,\mu_0,\phi-\phi_0;\tau_\lambda) \\ &\cong\frac{\mu_0E_{0,\lambda}}{E_{\lambda,x,y}(\mu_0;\tau_\lambda)} \\ &\quad\cdot\Bigg[e^{-\tau_\lambda/\mu_0}R_{\lambda,x,y}(-\mu,\mu_0,\phi-\phi_0) \\ &\qquad+2\pi\int_0^1 R_{\lambda,0,x,y}(-\mu,\mu')T_{\lambda,0}(-\mu_0,-\mu';\tau_\lambda)\,d\mu' \\ &\qquad+\pi\cos(\phi-\phi_0)\int_0^1 R_{\lambda,1,x,y}(-\mu,\mu') \\ &\qquad\cdot T_{\lambda,1}(-\mu_0,-\mu';\tau_\lambda)\,d\mu'\Bigg]+A^{hem}_{\lambda,x,y}(\mu_0;\tau_\lambda) \\ &\quad\cdot s_\lambda(\tau_\lambda)\cdot 2\int_0^1 R_{\lambda,0,x,y}(-\mu,\mu')\mu'\,d\mu' \end{aligned} \tag{24}$$

where $R_{\lambda,x,y}$ within the integrals has also been expanded in a two-term cosine series in $\phi-\phi'$

$$\begin{aligned} R_{\lambda,x,y}&(-\mu,\mu',\phi-\phi') \\ &=R_{\lambda,0,x,y}(-\mu,\mu')+R_{\lambda,1,x,y}(-\mu,\mu') \\ &\quad\cdot\cos(\phi-\phi'). \end{aligned} \tag{25}$$

After some rearranging, (24) can be used in an iterative scheme to determine $R_{\lambda,x,y}$. We have

$$\begin{aligned} R^{(n+1)}_{\lambda,x,y}&(-\mu,\mu_0,\phi-\phi_0) \\ &=\frac{E_{\lambda,x,y}(\mu_0;\tau_\lambda)}{\mu_0E_{0,\lambda}e^{-\tau_\lambda/\mu_0}}\cdot r_{\lambda,x,y}(-\mu,\mu_0,\phi-\phi_0;\tau_\lambda) \\ &\quad-\frac{2\pi}{e^{-\tau_\lambda/\mu_0}}\cdot\int_0^1 R^{(n)}_{\lambda,0,model}(-\mu,\mu') \\ &\quad\cdot T_{\lambda,0}(-\mu_0,-\mu';\tau_\lambda)\,d\mu'-\frac{\pi\cos(\phi-\phi_0)}{e^{-\tau_\lambda/\mu_0}} \\ &\quad\cdot\int_0^1 R^{(n)}_{\lambda,1,model}(-\mu,\mu')T_{\lambda,1}(-\mu_0,-\mu';\tau_\lambda)\,d\mu' \\ &\quad-\frac{A^{hem}_{\lambda,x,y}(\mu_0;\tau_\lambda)\cdot s_\lambda(\tau_\lambda)\cdot E_{\lambda,x,y}(\mu_0;\tau_\lambda)}{\mu_0E_{0,\lambda}e^{-\tau_\lambda/\mu_0}} \\ &\quad\cdot 2\int_0^1 R^{(n)}_{\lambda,0,model}(-\mu,\mu')\mu\,d\mu' \end{aligned} \tag{26}$$

where $R^{(n)}_{\lambda,0,x,y}$ and $R^{(n)}_{\lambda,1,x,y}$ are replaced by $R^{(n)}_{\lambda,0,model}$ and $R^{(n)}_{\lambda,1,model}$, respectively, which are produced from a

$$r_{\lambda,x,y}(-\mu,\mu_0,\phi-\phi_0;\tau_\lambda)=\frac{\displaystyle\int_0^1\int_0^{2\pi}R_{\lambda,x,y}(-\mu,\mu',\phi-\phi')L^{inc}_{\lambda,x,y}(\mu',\mu_0,\phi'-\phi_0;\tau_\lambda)\mu'\,d\mu'\,d\phi'}{E_{\lambda,x,y}(\mu_0;\tau_\lambda)} \tag{21}$$

parameterized BRF model. This step is necessary because $R_{\lambda,0,x,y}$ and $R_{\lambda,1,x,y}$ in the integrals of (24) are dependent on μ', the direction of incidence of the radiance at the surface, and this dependence is displayed in the MISR data only for the single direction μ_0, the cosine of the sun angle of the observations. The parameterized BRF model $R^{(n)}_{\lambda,model}$ is specified by fitting it to $R^{(n)}_{\lambda,x,y}$ at the MISR view angles and determining the best fit parameters. Once the parameters are determined, this procedure then allows $R^{(n)}_{\lambda,0,model}$ and $R^{(n)}_{\lambda,1,model}$ to be computed from the expressions

$$R^{(n)}_{\lambda,0,model}(-\mu,\mu') = \frac{1}{2\pi}\int_0^{2\pi} R^{(n)}_{\lambda,model}(-\mu,\mu',\phi-\phi')\,d\phi' \quad (27)$$

$$R^{(n)}_{\lambda,1,model}(-\mu,\mu')\cos(\phi-\phi_0) = \frac{1}{\pi}\int_0^{2\pi} R^{(n)}_{\lambda,model}(-\mu,\mu',\phi-\phi') \cdot\cos(\phi'-\phi_0)\,d\phi'. \quad (28)$$

The BRF model used is that of Rahman *et al.* [30], modified to allow a nearly linearizable least-squares fitting analysis. This modified model is described by

$$R_{\lambda,model}(-\mu,\mu_0,\phi-\phi_0) = r_{0,\lambda}\cdot[\mu\mu_0(\mu+\mu_0)]^{k_\lambda-1}\cdot\exp[b_\lambda\cdot p(\Omega)] \cdot h_\lambda(-\mu,\mu_0,\phi-\phi_0) \quad (29)$$

with three free parameters $r_{0,\lambda}$, k_λ, and b_λ. The function h_λ is a factor to account for the hot spot

$$h_\lambda(-\mu,\mu_0,\phi-\phi_0) = 1+\frac{1-r_{0,\lambda}}{1+G(-\mu,\mu_0,\phi-\phi_0)} \quad (30)$$

with

$$G(-\mu,\mu_0,\phi-\phi_0) = \left[\frac{1-\mu^2}{\mu^2}+\frac{1-\mu_0^2}{\mu_0^2}+2\frac{\sqrt{1-\mu^2}}{\mu}\cdot\frac{\sqrt{1-\mu_0^2}}{\mu_0}\cdot\cos(\phi-\phi_0)\right]^{1/2}. \quad (31)$$

The function p in (29) is assumed to depend only on the scattering angle Ω, the angle between the directions of the incident and reflected radiances and is defined to be

$$p(\Omega) = \cos\Omega = -\mu\mu_0+(1-\mu^2)^{1/2}\cdot(1-\mu_0^2)^{1/2}\cdot\cos(\phi-\phi_0). \quad (32)$$

The fitting of $R_{\lambda,model}$ to $R^{(n)}_{\lambda,x,y}$ is accomplished by first taking the logarithm of each function, differencing them, and then computing the sum of the squares of the residuals

$$S = \sum_i\left[\ln R^{(n)}_{\lambda,x,y}(-\mu_i,\mu_0,\phi_i-\phi_0) - \ln R^{(n)}_{\lambda,model}(-\mu_i,\mu_0,\phi_i-\phi_0)\right]^2 \quad (33)$$

where the summation is over the cameras used and

$$\ln R^{(n)}_{\lambda,model}(-\mu_i,\mu_0,\phi_i-\phi_0) = \ln r^{(n)}_{0,\lambda}+(k^{(n)}_\lambda-1)\cdot\ln[\mu_i\mu_0(\mu+\mu_0)] + b^{(n)}_\lambda\cdot p(\Omega_i)+\ln h^{(n)}_\lambda(-\mu_i,\mu_0,\phi_i-\phi_0). \quad (34)$$

The model is given explicit dependence on the iteration count through the superscript (n) because the parameters are updated every time $R^{(n)}_{\lambda,x,y}$ is iterated. Aside from the $\ln h^{(n)}_\lambda$ term in (34), we note that $\ln R_{\lambda,model}$ is linear in the three model parameters $\ln r_{0,\lambda}$, k_λ, and b_λ. The $\ln h^{(n)}_\lambda$ term is easily handled by simply using the value of $r_{0,\lambda}$ from the previous iteration

$$h^{(n)}_\lambda(-\mu,\mu_0,\phi-\phi_0) = 1+\frac{1-r^{(n-1)}_{0,\lambda}}{1+G(-\mu,\mu_0,\phi-\phi_0)} \quad (35)$$

where $r^{(-1)}_{0,\lambda}$ is set equal to zero. Once the parameters are found, $R^{(n)}_{\lambda,0,model}$ and $R^{(n)}_{\lambda,1,model}$ can be computed using (27) and (28).

As a good initial estimate to start the iteration, we set the BRF equal to the HDRF, i.e.,

$$R^{(0)}_{\lambda,x,y}(-\mu,\mu_0,\phi-\phi_0) = r_{\lambda,x,y}(-\mu,\mu_0,\phi-\phi_0;\tau_\lambda). \quad (36)$$

The iteration process expressed by (26) is then cycled until convergence is achieved. Convergence is measured by the metric D, defined as

$$D = \frac{1}{A^{hem}_{\lambda,x,y}(\mu_0;\tau_\lambda)}\cdot\left\{\sum_i\left[R^{(n+1)}_{\lambda,x,y}(-\mu_i,\mu_0,\phi_i-\phi_0 - R^{(n)}_{\lambda,x,y}(-\mu_i,\mu_0,\phi_i-\phi_0)\right]^2\right\}^{1/2} \quad (37)$$

where the summation is over the cameras used. When $D\le D_{thresh}$, a threshold value, the iteration process is terminated. Like the HDRF/BHR iteration process, this process is also very stable and efficient in achieving convergence.

Finally, the DHR $A^{dir}_{\lambda,x,y}$ is determined by directly integrating the BRF from the final iteration $R^{(N)}_{\lambda,x,y}$ over the hemisphere, assuming the azimuth angle model of (25)

$$A^{dir}_{\lambda,x,y}(\mu_0) = \frac{1}{\pi}\int_0^1\int_0^{2\pi} R_{\lambda,x,y}(-\mu,\mu_0,\phi-\phi_0)\mu\,d\mu\,d\phi = 2\int_0^1 R^{(N)}_{\lambda,0,x,y}(-\mu,\mu_0)\mu\,d\mu. \quad (38)$$

Since $R^{(N)}_{\lambda,x,y}$ is determined only at the MISR camera angles, $R^{(N)}_{\lambda,0,x,y}$ can be expressed as in (39), shown at the bottom of the next page, where ϕ_f and ϕ_a are the forward and aftward view azimuth angles for each symmetrically viewing camera pair.

VI. PAR-Integrated BHR and DHR

For radiation balance and climate studies, the shortwave (the effective wavelength range of the solar spectrum) BHR is needed, split into the PAR regime (400–700 nm) and the non-PAR regime (>700 nm). Since MISR has only four narrow bands in the shortwave region of the spectrum, additional information concerning the spectral shape of the surface BHR is needed to transform the four MISR spectral BHR's to a full shortwave BHR. This type of information can be obtained from other Earth Observing System (EOS) instruments, e.g., MODIS, and we leave the algorithm to retrieve it to the postlaunch era. However, since three of the four MISR bands are in the PAR spectral region, we include a PAR-integrated BHR and DHR as part of our at-launch surface product. They are a measure of the amount of incident PAR absorbed by the complete canopy-soil system and can be compared to FPAR, another MISR surface product parameter [10]. Unlike the surface products described so far, which are calculated for a subregion size of 1.1 km, these PAR-integrated albedos are calculated for the 17.6-km region.

The PAR-integrated BHR A^{hem}_{PAR} can be written as

$$A^{hem}_{PAR}(\mu_0;\,\tau_\lambda)=\frac{\displaystyle\int_{400}^{700}\langle M_\lambda(\mu_0;\,\tau_\lambda)\rangle\,d\lambda}{\displaystyle\int_{400}^{700}\langle E_\lambda(\mu_0;\,\tau_\lambda)\rangle\,d\lambda} \tag{40}$$

where

$$\langle M_\lambda(\mu_0;\,\tau_\lambda)\rangle=\frac{1}{N_{sub}}\sum_{x,\,y}M_{\lambda,\,x,\,y}(\mu_0;\,\tau_\lambda) \tag{41}$$

$$\langle E_\lambda(\mu_0;\,\tau_\lambda)\rangle=\frac{1}{N_{sub}}\sum_{x,\,y}E_{\lambda,\,x,\,y}(\mu_0;\,\tau_\lambda) \tag{42}$$

with the summation taken over the N_{sub} subregions within the 17.6-km region. The surface irradiance $E_{\lambda,\,x,\,y}$ is calculated from (8) and the radiant exitance $M_{\lambda,\,x,\,y}$ is calculated from (7), written as

$$M_{\lambda,\,x,\,y}(\mu_0;\,\tau_\lambda)=A^{hem}_{\lambda,\,x,\,y}(\mu_0;\,\tau_\lambda)\cdot E_{\lambda,\,x,\,y}(\mu_0;\,\tau_\lambda). \tag{43}$$

An identical calculation is done to obtain the PAR-integrated DHR A^{dir}_{PAR}, but with

$$E_{\lambda,\,x,\,y}(\mu_0)=\mu_0E_{0,\,\lambda} \tag{44}$$

$$M_{\lambda,\,x,\,y}(\mu_0)=A^{dir}_{\lambda,\,x,\,y}(\mu_0)\cdot\mu_0E_{0,\,\lambda}. \tag{45}$$

The spectral integration in (40) and its counterpart for A^{dir}_{PAR} is then carried out using a piecewise, linear curve to approximate the spectrum between the three MISR wavelengths contained within the integral. This enables the integrals to be replaced by weighted sums of the spectral parameters, with the weights being preestablished. Details of this procedure can be found in [26].

VII. Surface Radiation Parameters

The spectral HDRF and BHR and the spectral BRF and DHR, retrieved by means of the algorithms described in Sections IV and V, are archived as part of the MISR standard surface product. Additional parameters, not explicitly archived, but which can be easily calculated from the standard aerosol and surface parameters, include the following:

1) surface spectral irradiance $E_{\lambda,\,x,\,y}$ (incident radiant flux density or flux) for the ambient atmosphere, given by (8), and for no atmosphere, given by (44);
2) surface spectral radiant exitance $M_{\lambda,\,x,\,y}$ (exiting radiant flux density or flux) for the ambient atmosphere, given by (43), and for no atmosphere, given by (45);
3) surface-leaving spectral radiance $L^{surf}_{\lambda,\,x,\,y}$ for the ambient atmosphere

$$L^{surf}_{\lambda,\,x,\,y}(-\mu,\,\mu_0,\,\phi-\phi_0;\,\tau_\lambda)=\frac{1}{\pi}\cdot r_{\lambda,\,x,\,y}(-\mu,\,\mu_0,\,\phi-\phi_0;\,\tau_\lambda)E_{\lambda,\,x,\,y}(\mu_0;\,\tau_\lambda) \tag{46}$$

where (4) and (5) were used and for no atmosphere

$$L^{surf}_{\lambda,\,x,\,y}(-\mu,\,\mu_0,\,\phi-\phi_0;\,\tau_\lambda)=\frac{1}{\pi}\cdot R_{\lambda,\,x,\,y}(-\mu,\,\mu_0,\,\phi-\phi_0)\mu_0E_{0,\,\lambda} \tag{47}$$

where (2) and (22) were used.

VIII. Surface Characterization Parameters

The surface products discussed so far are very basic and are retrieved using straightforward techniques, rooted in well developed 1-D radiative transfer theory of the atmosphere/surface boundary problem. The advanced MISR surface products, which include a biome-based surface description or classification, LAI, and FPAR, require a more sophisticated approach to their retrieval. The algorithm used to determine these three products uses as input the retrieved spectral BHR and BRF/DHR products, described in Sections IV and V. Fundamental to the operation of the algorithm is the use of precomputed radiation parameters, which are derived from 3-D modeling of complex vegetation canopies and their underlying surface (see [31]) and stored in a lookup table labeled the Canopy Architecture Radiative Transfer (CART) file [26]. These precomputed parameters allow a fast and accurate computation of BHR and BRF/DHR values at the top of the canopy for a wide variety of canopy/soil models, in which biome type, LAI, and soil reflectance can vary.

The algorithm provides a comparison of the retrieved and modeled reflectances and reflectance factors, using a two-step procedure. First, the retrieved BHR and DHR in the four MISR spectral bands are compared to the corresponding modeled values, which are a function of biome type,

$$R^{(N)}_{\lambda,\,0,\,x,\,y}(-\mu,\,\mu_0)=\frac{R^{(N)}_{\lambda,\,x,\,y}(-\mu,\,\mu_0,\,\phi_a-\phi_0)\,\cos(\phi_f-\phi_0)-R^{(N)}_{\lambda,\,x,\,y}(-\mu,\,\mu_0,\,\phi_f-\phi_0)\,\cos(\phi_a-\phi_0)}{\cos(\phi_f-\phi_0)-\cos(\phi_a-\phi_0)} \tag{39}$$

LAI, and soil reflectance. Only for those models that pass this comparison test is a second comparison test performed between the retrieved spectral BRF values and the modeled values. The canopy/soil models that pass this second test are considered to be successful representations of the actual canopy/soil condition. A weighted average LAI and its spread are calculated for each biome type of the successful models. The biome type with the minimum spread in LAI is then used to calculate FPAR. The algorithm considers six distinct biome types for the models—grasses and cereal crops, semiarid shrublands, broadleaf crops, savanna, broadleaf forest, and needle leaf forest. Two additional and nonvegetative surface classifications include the categories water and barren. Land subregions are classified as barren when the NDVI is less than a threshold value and, consequently, LAI and FPAR are both set to zero. Additional information and details about this algorithm can be found in [10] and [26].

By introducing more realism into the modeling of the canopy architecture and subsequent radiative transfer process, this algorithm represents a significant advancement in the effort to retrieve canopy biophysical parameters. One current method to determine FPAR, for example, is based on a biome-dependent, simple linear relationship between FPAR and the vegetation index [32], [33], which ignores much of the variation in canopy architecture and soil reflectance inherent in real canopies. We view the physically based MISR LAI/FPAR algorithm as a first step toward future algorithms that will be designed to retrieve a larger list of canopy biophysical products.

IX. Surface Retrieval Simulations

The accuracy of the HDRF/BHR and BRF/DHR retrieval algorithms was studied by applying them to simulated MISR radiance data. These radiances were computed using a number of different, directionally reflecting, surface types, overlain by an atmosphere containing aerosols. The bidirectional reflectance factors describing the model surface reflection properties were derived from measurements of 11 distinct types of natural surfaces in the two AVHRR wavelength bands 1 (0.58–0.67 μm) and 2 (0.73–1.1 μm) [34]–[36]. These measurements are especially useful in modeling work because of the fairly complete angular coverage in both the view and sun directions. It should be noted that the reported measurements are actually HDRF's, i.e., no correction was made for atmospheric effects, but in our study, we treated the measurements as BRF's when modeling the TOA radiances. This approximation is not significant since we are primarily interested in the variety of angular shapes and reflectance values that the measurements offer. We also assumed that the AVHRR bands 1 and 2 were equivalent to the MISR red and near-infrared bands at 672 and 866 nm, respectively, for each of the derived BRF models. The 11 surface types are listed in Table I along with their BHR at 672 nm.

The atmospheric model used for the simulated MISR radiance calculations contains both Rayleigh and aerosol scattering. The selected aerosol was a sulfate/nitrate type at 70% relative humidity (RH) with an effective particle radius of 0.21 μm and with a phase function described by an asymmetry parameter of 0.68 and a single-scattering albedo of 1.0 at a wavelength of 672 nm. The aerosol was distributed in the atmosphere with a particle density scale height of 2 km. A number of aerosol turbidity conditions were investigated, ranging from a light aerosol load (optical depth of 0.1 at 672 nm) to a relatively heavy load (optical depth of 0.4). The simulated data were calculated for three solar zenith angles ($\theta_0 = 25$, 45, and 65°) and three MISR azimuth angle differences ($\Delta\phi = 30$, 60, and 90°), as measured from the principal plane. The radiative transfer calculations were done using a multiple scattering, matrix-operator technique [37], which included all of the interactions between the surface and the atmosphere.

TABLE I
Surface Models

Case	Surface Type	BRF (672 nm)
1	Soil	0.186
2	Grassland	0.318
3	Steppe Grass	0.211
4	Hard Wheat	0.228
5	Irrigated Wheat	0.063
6	Hardwood Forest	0.035
7	Pine Forest	0.038
8	Lawn Grass	0.058
9	Corn	0.082
10	Soybean	0.034
11	Orchard Grass	0.077

Three different scenarios were studied to test the sensitivity of the HDRF retrieval to atmospheric conditions. The first was the use of the correct aerosol type and column amount in the retrieval process to gauge how well the algorithm works under optimum conditions. Next, the correct aerosol type was used, but the column amount was decreased a bit from the true value. Finally, the correct aerosol column amount was used, but the aerosol type was modified by increasing the RH from 70 to 99%, thus increasing the particle effective radius to 0.64 μm. To gauge the performance of the HDRF/BHR retrieval algorithm, we define a metric $\delta_{\lambda,x,y}$, the average HDRF deviation, as

$$\delta_{\lambda,x,y}(\tau_\lambda) = \tfrac{1}{9} \cdot \sum_i \left| r_{\lambda,x,y}(-\mu_i, \mu_0, \phi_i - \phi_0; \tau_\lambda) - r^{true}_{\lambda,x,y}(-\mu_i, \mu_0, \phi_i - \phi_0; \tau_\lambda) \right| \quad (48)$$

where $r_{\lambda,x,y}$ and $r^{true}_{\lambda,x,y}$ are the retrieved and true HDRF, respectively, and the summation is over the nine MISR camera angles. Fig. 1 shows the HDRF retrieval results of the 11 surface cases at 672 nm for $\theta_0 = 45°$ and all three $\Delta\phi$, using the correct aerosol type (sulfate/nitrate at RH 70%) and column amount (optical depth of 0.4). It is apparent from this figure that the retrieval accuracy is approximately proportional to the reflectance level of the surface. This is

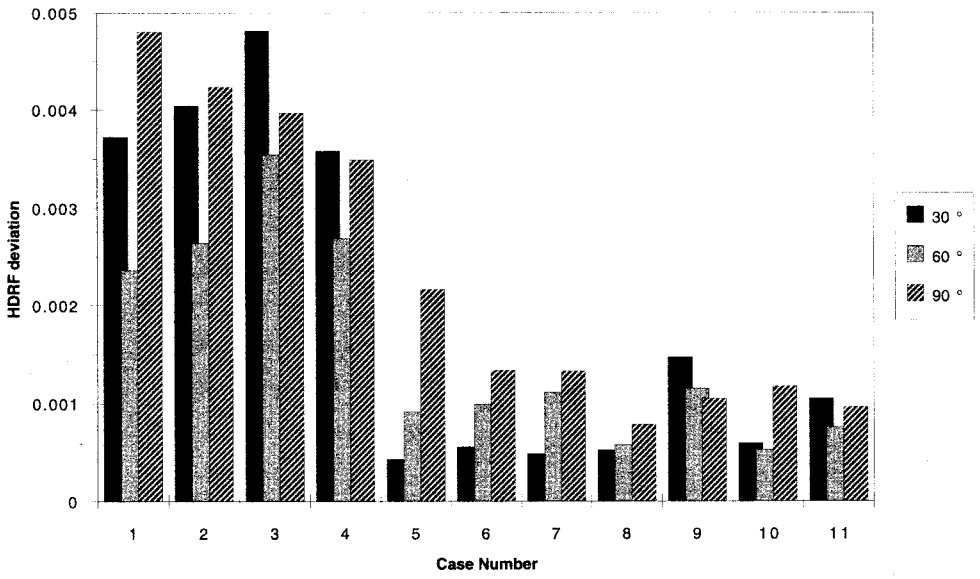

Fig. 1. Accuracy of HDRF's retrieved from simulated MISR data for 11 surface cases and three viewing geometries (azimuth angle from the principal plane is $\Delta\phi = 30, 60,$ and $90°$, all at solar zenith angle $\theta_0 = 45°$). The correct aerosol properties were used in the retrieval process (type is sulfate/nitrate at RH 70% with an optical depth of 0.4).

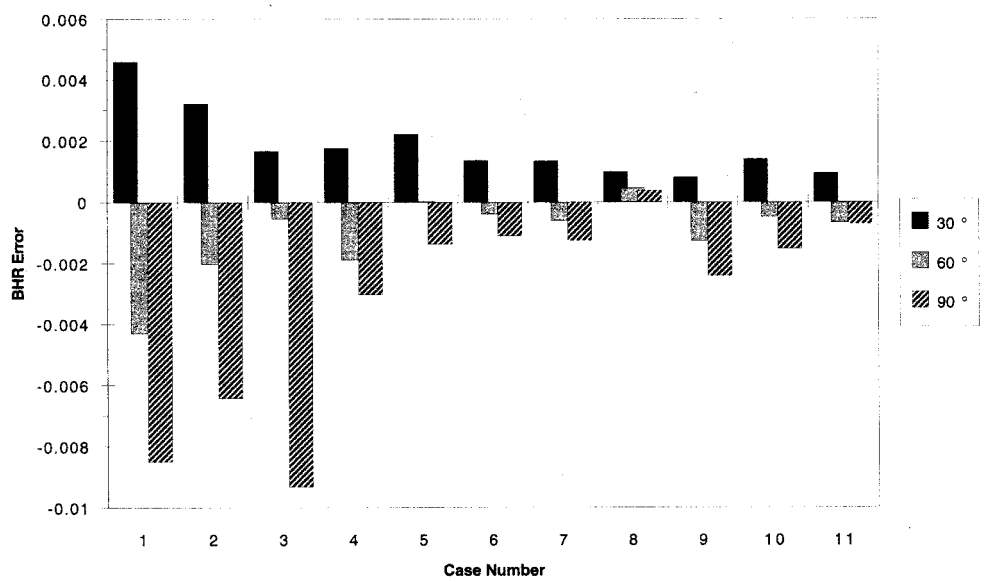

Fig. 2. Accuracy of BHR's retrieved from simulated MISR data for 11 surface cases and three viewing geometries (azimuth angle from the principal plane is $\Delta\phi = 30, 60,$ and $90°$, all at solar zenith angle $\theta_0 = 45°$). The correct aerosol properties were used in the retrieval process (type is sulfate/nitrate at RH 70% with an optical depth of 0.4).

clearly demonstrated by the relatively large average deviations of the first four cases compared to the others and the similar pattern exhibited by the BHR listed in Table I. Also apparent is the fact that the retrieval accuracy does not depend strongly on $\Delta\phi$, the azimuth angle difference between the plane of the measurements and the principal plane, although there is a tendency toward less accurate retrievals when $\Delta\phi$ is near $90°$. In general, the average deviation is about 2% of the BHR value, indicating the high intrinsic accuracy of the HDRF/BHR retrieval algorithm under optimum conditions. Similar results were found for the retrievals at the other two solar zenith angles $\theta_0 = 25°$ and $65°$. The BHR retrieval results corresponding to the HDRF results of Fig. 1 are shown in Fig. 2. Here, the metric used to describe the BHR retrieval accuracy is the BHR error $\varepsilon_{\lambda,x,y}$, defined as

$$\varepsilon_{\lambda,x,y}(\tau_\lambda) = A^{hem}_{\lambda,x,y}(\mu_0;\tau_\lambda) - A^{hem,true}_{\lambda,x,y}(\mu_0;\tau_\lambda) \quad (49)$$

where $A^{hem}_{\lambda,x,y}$ and $A^{hem,true}_{\lambda,x,y}$ are the retrieved and true values, respectively. Comparison of Figs. 1 and 2 shows that the BHR error is typically somewhat larger than the average HDRF deviation, indicative of the fact that the BHR integration over the upward-directed hemisphere includes large amounts of solid angle where no measurements are obtained. However, the overall uncertainty in the retrieved BHR is generally less

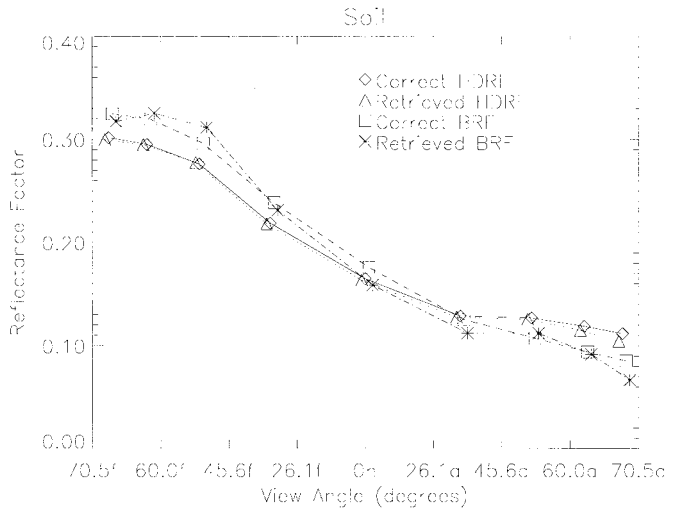

Fig. 3. Correct and retrieved soil (case 1) reflectance factors versus MISR view zenith angle. The solar zenith angle is $\theta_0 = 45°$, and the azimuth angle from the principal plane is $\Delta\phi = 30°$. The correct aerosol properties were used in the retrieval process (type is sulfate/nitrate at RH 70% with an optical depth of 0.4).

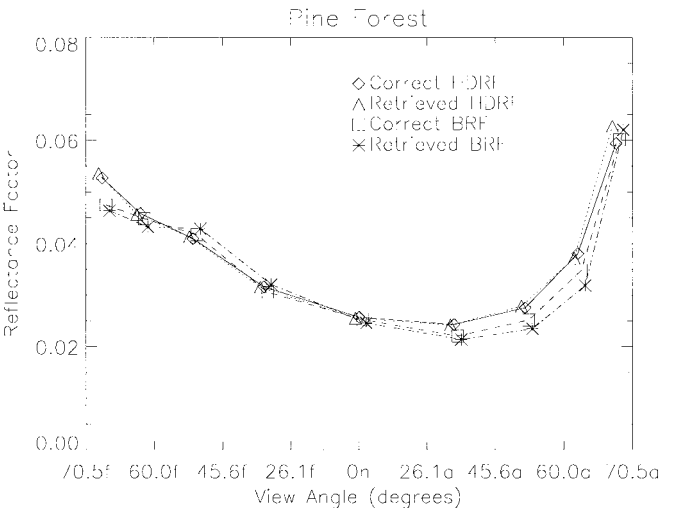

Fig. 5. Correct and retrieved pine forest (case 7) reflectance factors versus MISR view zenith angle. The solar zenith angle is $\theta_0 = 45°$, and the azimuth angle from the principal plane is $\Delta\phi = 30°$. The correct aerosol properties were used in the retrieval process (type is sulfate/nitrate at RH 70% with an optical depth of 0.4).

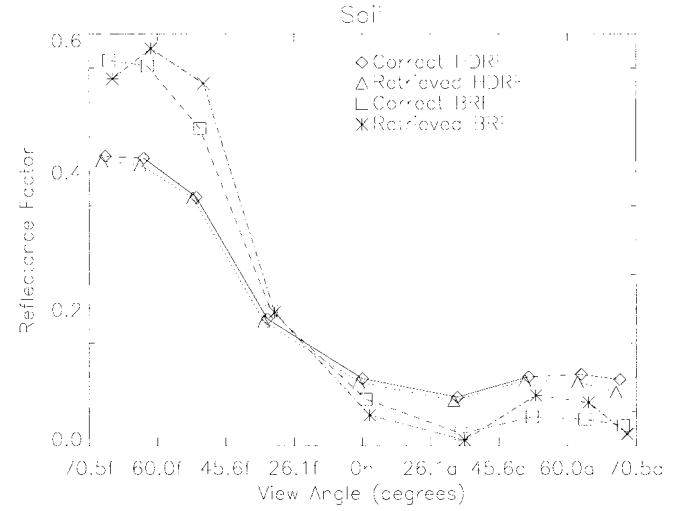

Fig. 4. Same as Fig. 3, except the solar zenith angle is $\theta_0 = 65°$.

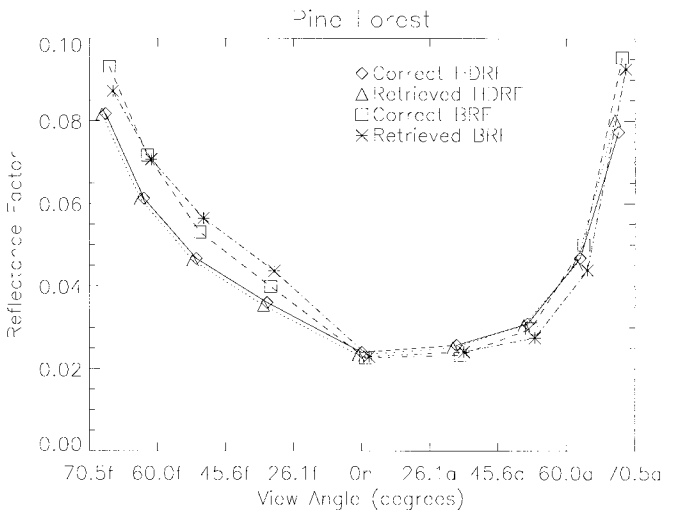

Fig. 6. Same as Fig. 5, except the solar zenith angle is $\theta_0 = 65°$.

than 5% for all of the solar and viewing geometries considered in this study.

Figs. 3 and 4 show the HDRF and BRF retrieval at 672 nm as a function of the MISR camera view zenith angles for surface case 1 (soil), an aerosol optical depth of 0.4, $\Delta\phi = 30°$, and solar zenith angles $\theta_0 = 45$ and 65°, respectively. The HDRF and BRF retrieval for surface case 7 (pine forest) under the same atmospheric and sun-view conditions are shown in Figs. 5 and 6. The difference between the HDRF and BRF generally increases with increasing optical depth; Figs. 3–6 show that this difference also increases with increasing solar zenith angle. The BRF retrieval is noticeably less accurate than the HDRF retrieval, but nevertheless, produces a very acceptable result.

All results presented up to now were obtained using the correct aerosol type and amount. However, a certain amount of error or uncertainty is inevitable when an aerosol retrieval is performed using the MISR data [23]. For optical depths less than 0.5, the expected optical depth uncertainty will be about 0.05, with a possibility for misidentification of aerosol type. To determine the impact of these types of errors on the accuracy of the surface retrievals, the properties of the aerosol model used in the retrievals were allowed to deviate from those of the correct model. First, we modified the aerosol column amount, using an optical depth of 0.35 instead of the correct value of 0.4 in the surface retrieval algorithm. The HDRF retrieval results, shown in Fig. 7, and the BHR results, shown in Fig. 8, for $\theta_0 = 45°$ should be compared to those in Figs. 1 and 2. We note that the average HDRF deviation in Fig. 7 is about 0.01 for each surface case. This is approximately 2.5 times larger than the average deviations in Fig. 1 for the first four cases and approximately ten times larger for the remaining cases,

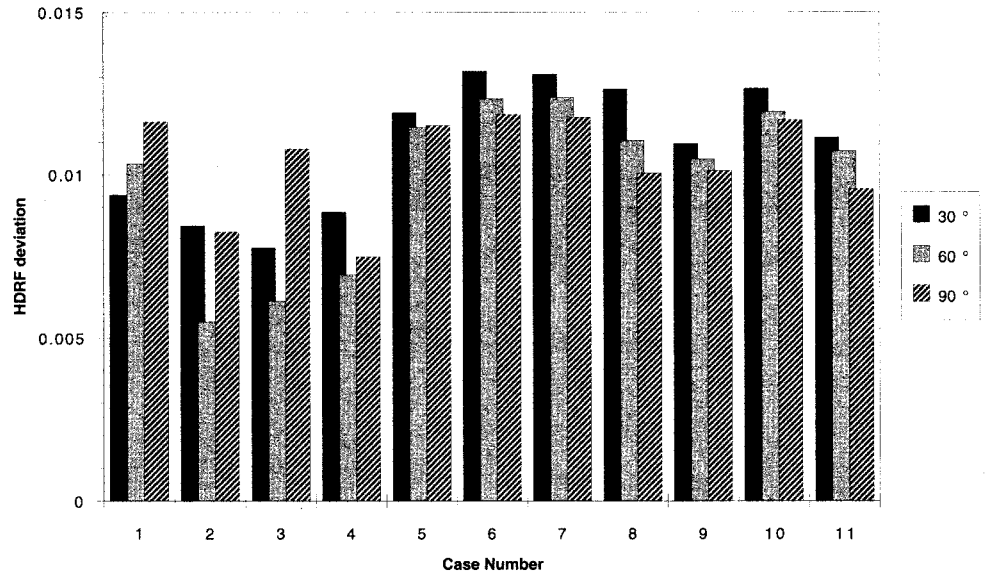

Fig. 7. Accuracy of HDRF's retrieved from simulated MISR data for 11 surface cases and three viewing geometries (azimuth angle from the principal plane is $\Delta\phi = 30, 60,$ and $90°$, all at solar zenith angle $\theta_0 = 45°$). The correct aerosol type (sulfate/nitrate at RH 70%) and an incorrect optical depth of 0.35 were used in the retrieval process.

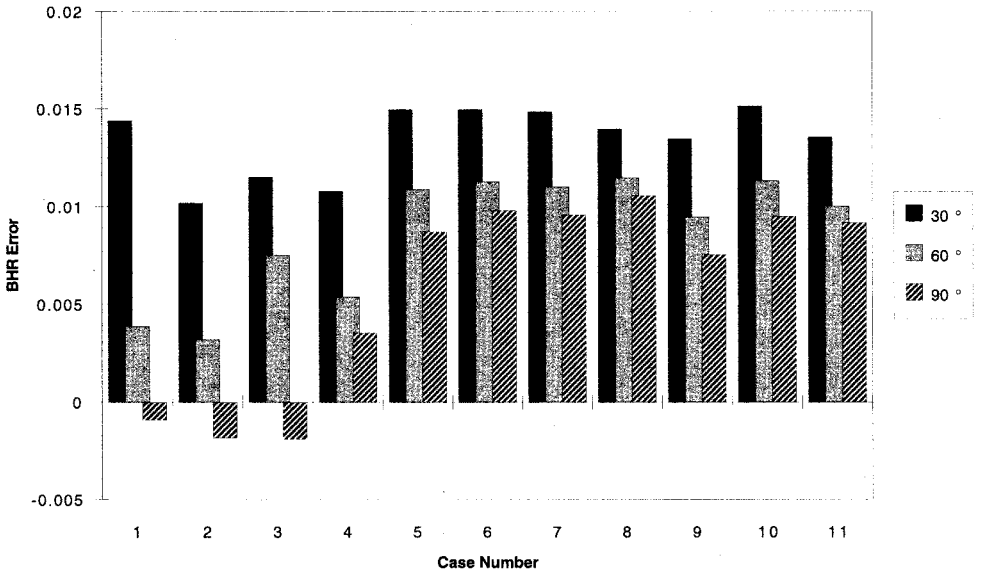

Fig. 8. Accuracy of BHR's retrieved from simulated MISR data for 11 surface cases and three viewing geometries (azimuth angle from the principal plane is $\Delta\phi = 30, 60,$ and $90°$, all at solar zenith angle $\theta_0 = 45°$). The correct aerosol type (sulfate/nitrate at RH 70%) and an incorrect optical depth of 0.35 were used in the retrieval process.

which have a much smaller BHR. Also, the BHR errors in Fig. 8 are now positively biased by more than 0.01, compared to those in Fig. 2, a result of using too small an optical depth.

Another example of the consequences of using an inaccurate aerosol model is the case in which the correct optical depth is used, but with a modified aerosol type (sulfate/nitrate at RH 99% instead of 70%). The results of the HDRF and BHR retrieval for this case are displayed in Figs. 9 and 10, respectively. Again, the results are biased by amounts that are much larger than the inherent accuracy of the HDRF/BHR retrieval process, as illustrated in Figs. 1 and 2. Clearly, it is the accuracy of the aerosol retrieval process that will be the limiting factor in determining the degree of uncertainty in many of the surface products.

The results presented in Figs. 1–10 are for an aerosol amount described by an optical depth of 0.4 at 672 nm. Retrievals on simulated data with smaller optical depths show correspondingly smaller errors. However, the projected 0.05 uncertainty in optical depth for MISR aerosol retrievals, even when the optical depth is small, will produce biases in the HDRF and BHR retrievals that are comparable to those observed in Figs. 7 and 8. Expressions for the formal uncertainties of the retrieved HDRF and BHR, which include the effects of uncertainties in the aerosol properties, can be

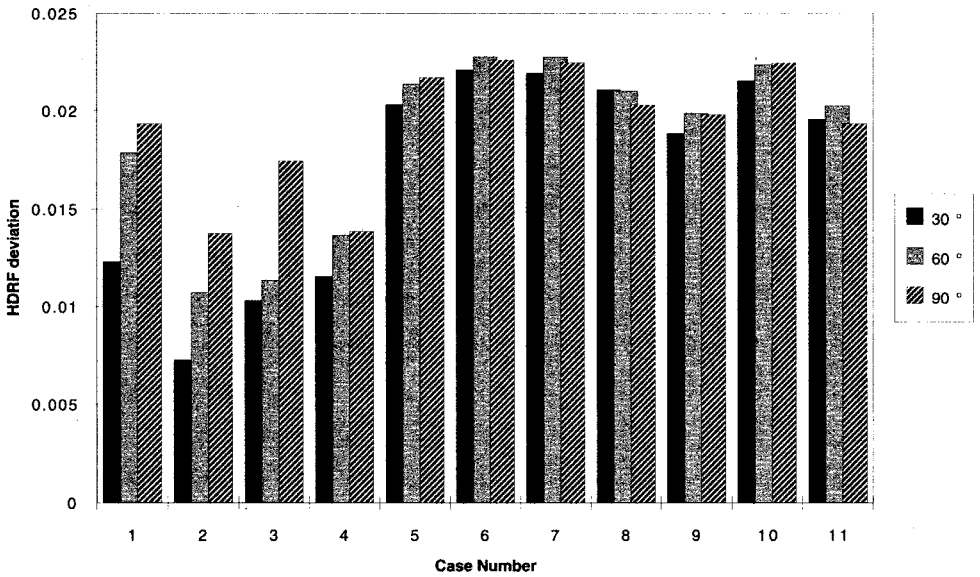

Fig. 9. Accuracy of HDRF's retrieved from simulated MISR data for 11 surface cases and three viewing geometries (azimuth angle from the principal plane is $\Delta\phi = 30, 60$, and $90°$, all at solar zenith angle $\theta_0 = 45°$). An incorrect aerosol type (sulfate/nitrate at RH 99%) and the correct optical depth of 0.4 were used in the retrieval process.

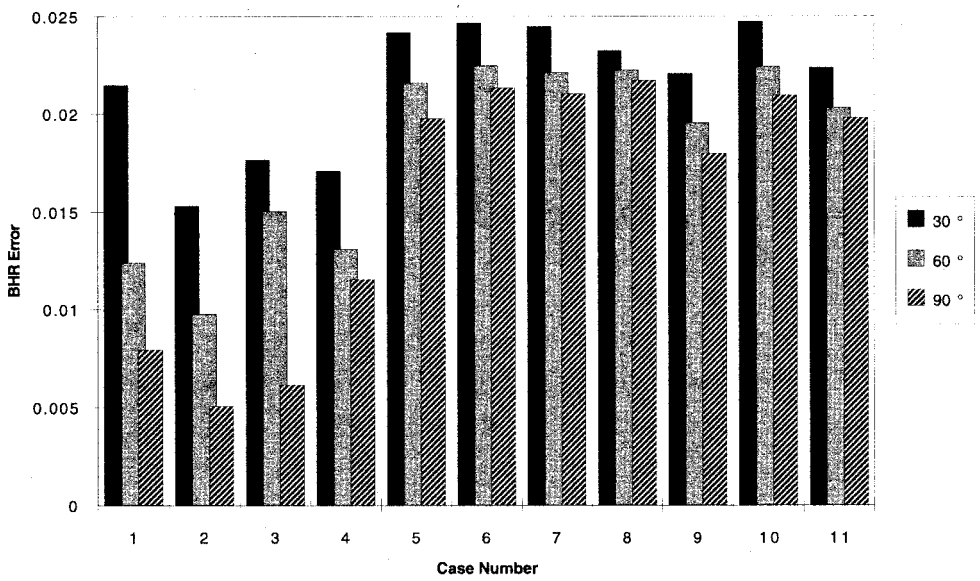

Fig. 10. Accuracy of BHR's retrieved from simulated MISR data for 11 surface cases and three viewing geometries (azimuth angle from the principal plane is $\Delta\phi = 30, 60$, and $90°$, all at solar zenith angle $\theta_0 = 45°$). An incorrect aerosol type (sulfate/nitrate at RH 99%) and an incorrect optical depth of 0.4 were used in the retrieval process.

found in [26]. These uncertainty estimates will be archived as part of the MISR standard data products.

X. Discussion

The retrieval techniques described in Sections IV, V, and VIII form the core of the MISR surface product algorithms. They take full advantage of the multiangle nature of the MISR data sets, allowing a more accurate determination of the surface directional reflectance properties than can be obtained with conventional single-view instruments. For example, if the surface-leaving radiance $L^{surf}_{\lambda,x,y}$ is to be retrieved from single-view data, it would be computed using (11), an expression based on the assumption of a Lambertian surface. This expression, however, is only approximate and describes just the initial estimate of $L^{surf}_{\lambda,x,y}$ in the iteration procedure used by the MISR multiangle HDRF/BHR retrieval algorithm. This algorithm and the BRF/DHR algorithm are designed to accommodate MISR data without a full complement of nine view angles, due to possible cloud contamination or instrument problems in one or more cameras. Quality assessment parameters, which include information on the number of camera views used in the retrieval process, are archived to help assess the accuracy of the surface products.

Once the spectral HDRF and BHR are retrieved for a land subregion, they are then used as inputs to additional algorithms

TABLE II
SUMMARY OF MISR SURFACE PRODUCTS

Product name	Horizontal sampling (Coverage)	Comments
Hemispherical- Directional Reflectance Factor (HDRF)	1.1 km (Land)	• Surface radiance ratioed to that from ideal lambertian reflector at surface •Ambient sky conditions, i.e., direct plus diffuse illumination • 9 viewing angles, 4 spectral bands
BihemisphericalReflectance (BHR)	1.1 km spectral, 17.6 km PAR (Land)	• Radiant exitance ratioed to irradiance at surface (i.e. albedo) • Ambient sky conditions, i.e., direct plus diffuse illumination • 4 spectral bands and PAR integrated
Bidirectional Reflectance Factor (BRF)	1.1 km (Land)	• Surface radiance ratioed to that from ideal lambertian reflector at surface • Direct illumination only (no atmosphere) • 9 viewing angles, 4 spectral bands
BRF Model Parameters	1.1 km (Land	• Model parameters from a fit to the surface BRF
Directional-Hemispherical Reflectance (DHR)	1.1 km spectral, 17.6 km PAR (Land)	• Radiant exitance ratioed to irradiance at surface (albedo) • Direct illumination only • 4 spectral bands and PAR-integrated
Surface classification	1.1 km (Land)	• Selected from six major biome types plus two non-vegetated types • Determined using physically-based algorithm
NDVI	1.1 km (Land)	• Computed from retrieved spectral DHR
Leaf area index (LAI)	1.1 km (Land)	• Determined using physically-based algorithm
Fractional Absorbed Photosynthetically Active Radiation (FPAR)	17.6 km (Land)	• Determined using physically-based algorithm
Water-leaving radiances	1.1 km (Tropical Ocean)	• Most glitter-free B-camera viewing angle, blue and green spectral bands, low latitudes, using HDRF and conventional algorithms
Phytoplankton Pigment Concentration	1.1 km (Tropical Ocean)	• Calculated from water-leaving radiances

to retrieve the BRF and DHR, the PAR-integrated BHR and DHR, and the surface classification, the LAI, and the FPAR. When the surface retrieval is done for ocean samples, however, only the spectral HDRF is determined. For oceans, the surface-leaving radiance can be expressed as

$$L^{surf}_{\lambda,x,y}(-\mu,\mu_0,\phi-\phi_0;\tau_\lambda) = L^{water}_{\lambda,x,y}(-\mu,\mu_0,\phi-\phi_0;\tau_\lambda) + L^{glitter}_{\lambda,x,y}(-\mu,\mu_0,\phi-\phi_0;\tau_\lambda) \quad (50)$$

where $L^{water}_{\lambda,x,y}$ is the water-leaving radiance, which is that part of the radiance incident on the surface that penetrates the surface, scatters within the water proper, and then exits the surface, and $L^{glitter}_{\lambda,x,y}$ is the radiance reflected directly from the surface (Fresnel scattering) [38] and a contribution due to whitecaps [39]. When the aerosol retrieval is performed, the component of the TOA radiance due to $L^{glitter}_{\lambda,x,y}$,

$$L^{TOA,glitter}_{\lambda,x,y}(-\mu,\mu_0,\phi-\phi_0;\tau_\lambda) = e^{-\tau_\lambda/\mu}\cdot L^{glitter}_{\lambda,x,y}(-\mu,\mu_0,\phi-\phi_0;\tau_\lambda) + \int_0^1\int_0^{2\pi} T_\lambda(-\mu,-\mu',\phi-\phi';\tau_\lambda) \cdot L^{glitter}_{\lambda,x,y}(-\mu',\mu_0,\phi'-\phi_0;\tau_\lambda)\,d\mu'\,d\phi' \quad (51)$$

is also determined, based on precomputed values contained in the SMART data set. Therefore, the iteration procedure of the HDRF algorithm, expressed by (14), becomes an algorithm for retrieving $L^{water}_{\lambda,x,y}$ instead of $L^{surf}_{\lambda,x,y}$ by setting L^{atm}_λ in the expression equal to the sum of L^{atm}_λ and $L^{TOA,glitter}_{\lambda,x,y}$. Although $L^{water}_{\lambda,x,y}$ is retrieved for all nine MISR view angles, only the most glitter-free of the two radiances at 45.6° zenith angle will be archived. Also, these radiances will be retrieved only for the two spectral bands at 446 and 558 nm; $L^{water}_{\lambda,x,y}$

for the other two spectral bands are assumed to be zero. These two single-view radiances are then used to determine the phytoplankton pigment concentration, based on an algorithm developed for the CZCS [40]. There are alternative, more conventional, ways of determining $L_{\lambda,x,y}^{water}$, based on single-view satellite data. In particular, this product is currently being produced from SeaWiFS data using an algorithm [12] that is a prototype for the one under development for MODIS [11], an instrument on the same platform as MISR. A modified version of this algorithm will be used with MISR data, in addition to the HDRF algorithm, so that the two sets of results can be compared.

Validation of the MISR surface products will rely on several sources of data, including radiometrically calibrated aircraft observations, together with field observations of downwelling diffuse sky spectral radiance and irradiance, the direct solar spectral irradiance, and surface spectral HDRF. Details on planned field campaigns, experimental methodologies, and instrument calibration and data reduction procedures are documented in [41] and [42]. As the surface retrieval simulations have demonstrated, the accuracy of the MISR surface products (and the surface products from other spacecraft instruments) depends heavily on how well the aerosol properties are known. This requirement on accuracy also applies to the surface radiation parameters, described in Section VII, which can be derived from the MISR products. Thus, the validation plan is structured around the requirement of obtaining measurement sets from which aerosol and surface properties can be determined together.

XI. Concluding Remarks

By monitoring the global environment via multiangle, spectral imagery, MISR will make unique contributions to earth system science research. It will produce a number of surface data products (see Table II) on a daily basis that will be of interest to people in research disciplines covering broad areas of land, ocean, and atmospheric science. Using atmospheric information archived during the aerosol retrieval process, surface radiometric quantities, e.g., the spectral radiances and radiant flux densities, can also be determined from these surface products. We anticipate other progressions to new and more advanced products through ingestion of non-MISR data and the development of improved algorithms.

For further information about the MISR surface retrieval algorithms, refer to the MISR Algorithm Theoretical Basis documents, which can be found at the EOS Project Science Office website located at *http://eospso.gsfc.nasa.gov*.

Acknowledgment

The authors are grateful to B. Rheingans for his assistance with the graphical work and the reviewers for their constructive comments.

References

[1] R. E. Dickinson, "Land surface processes and climate-surface albedos and energy balance," *Adv. Geophys.*, vol. 25, pp. 305–353, 1981.

[2] D. S. Kimes, P. J. Sellers, and D. J. Diner, "Extraction of spectral hemispherical reflectance (albedo) of surfaces from nadir and directional reflectance data," *Int. J. Remote Sensing*, vol. 8, no. 12, pp. 1727–1746, 1987.

[3] P. J. Sellers, "Canopy reflectance, photosynthesis and transpiration," *Int. J. Remote Sensing*, vol. 6, no. 8, pp. 1335–1372, 1985.

[4] ——, "Canopy reflectance, photosynthesis and transpiration II: The role of biophysics in the linearity of their interdependence," *Remote Sens. Environ.*, vol. 21, pp. 143–183, 1987.

[5] J. Charney, W. J. Quirk, S. Chow, and J. Kornfield, "A comparative study of the effects of albedo change on droughts in semi-arid regions," *J. Atmos. Sci.*, vol. 34, pp. 1366–1385, 1977.

[6] R. E. Dickinson, B. Pinty, and M. M. Verstraete, "Relating surface albedos in GCM to remotely sensed data," *Agr. Forest Meteorol.*, vol. 52, pp. 109–131, 1990.

[7] Y. Mintz, *The Global Climate*, J. T. Houghton, Ed. Cambridge, U.K.: Cambridge Univ. Press, 1984.

[8] G. P. Asner, B. H. Braswell, D. S. Schimel, and C. A. Wessman, "Ecological research needs from multiangle remote sensing data," *Rem. Sens. Environ.*, vol. 63, no. 2, pp. 155–165, 1998.

[9] D. J. Diner, J. C. Beckert, T. H. Reilly, C. J. Bruegge, J. E. Conel, R. A. Kahn, J. V. Martonchik, T. P. Ackerman, R. Davies, S. A. W. Gerstl, H. R. Gordon, J.-P. Muller, R. B. Myneni, P. J. Sellers, B. Pinty, and M. M. Verstraete, "Multi-angle Imaging SpectroRadiometer instrument description and experiment overview," this issue, pp. 1072–1087.

[10] Y. Knyazikhin, J. V. Martonchik, D. J. Diner, R. B. Myneni, M. M. Verstraete, B. Pinty, and N. Gobron, "Estimation of vegetation canopy leaf area index and fraction of absorbed photosynthetically active radiation from atmosphere-corrected MISR data," *J. Geophys. Res.*, to be published.

[11] H. R. Gordon, *MODIS Normalized Water-Leaving Radiance Algorithm Theoretical Basis Document*, version 2, NASA, Langley, VA, submitted under NASA/GSFC Contract NAS5-31363, 1994.

[12] H. R. Gordon and M. Wang, "Retrieval of water-leaving radiance and aerosol optical thickness over the oceans with SeaWiFS: A preliminary algorithm," *Appl. Opt.*, vol. 33, pp. 443–452, 1994.

[13] S. Chandrasekhar, *Radiative Transfer*. New York: Dover, 1960.

[14] F. Cavayas, "Modeling and correction of topographic effect using multitemporal satellite images," *Can. J. Remote Sensing*, vol. 13, no. 2, pp. 49–67, 1987.

[15] P. M. Teillet, B. Guindon, and D. G. Goodenough, "On the slope-aspect correction of multispectral scanner data," *Can. J. Remote Sensing*, vol. 8, no. 2, pp. 84–106, 1982.

[16] R. J. Woodham and T. K. Lee, "Photometric method for radiometric correction of multispectral scanner data," *Can. J. Remote Sensing*, vol. 11, no. 2, pp. 132–161, 1985.

[17] M. H. Gray, "Radiometric correction of satellite imagery for topographic and atmospheric effects," M.Sc. thesis, Faculty of Forestry, Univ. British Columbia, Vancouver, BC, Canada, 1986.

[18] P. N. Reinersman and K. L. Carder, "Monte Carlo simulation of the atmospheric point-spread function with an application to correction for the adjacency effect," *Appl. Opt.*, vol. 34, no. 21, pp. 4453–4471.

[19] D. J. Diner and J. V. Martonchik, "Influence of aerosol scattering on atmospheric blurring of surface features," *IEEE Trans. Geosci. Remote Sensing*, vol. GE-23, pp. 618–624, Sept. 1985.

[20] ——, "Atmospheric transfer of radiation above an inhomogeneous non-Lambertian reflective ground. I. Theory," *J. Quant. Spectrosc. Radiat. Trans.*, vol. 31, no. 2, pp. 97–125, 1984.

[21] ——, "Atmospheric transfer of radiation above an inhomogeneous non-Lambertian reflective ground. II. Computational considerations and results," *J. Quant. Spectrosc. Radiat. Trans.*, vol. 32, no. 4, pp. 279–304, 1984.

[22] D. J. Diner, J. V. Martonchik, E. D. Danielson, and C. J. Bruegge, "Atmospheric correction of high resolution land surface images," in *Proc. IGARSS'89 Symp.*, Vancouver, BC, Canada.

[23] J. V. Martonchik, D. J. Diner, R. A. Kahn, T. P. Ackerman, M. M. Verstraete, B. Pinty, and H. R. Gordon, "Techniques for the retrieval of aerosol properties over land and ocean using multiangle imaging," this issue, pp. 1212–1227.

[24] D. J. Diner, W. A. Abdou, H. R. Gordon, R. A. Kahn, Y. Knjazikhin, J. V. Martonchik, S. McMuldroch, R. B. Myneni, and R. A. West, *Level 2 Ancillary Products and Datasets Algorithm Theoretical Basis*, Jet Propul. Lab., Pasadena, CA, vol. JPL D-13402, rev. A, 1997.

[25] P. J. Starks, J. M. Norman, B. L. Blad, E. A. Walter-Shea, and C. L. Walthal, "Estimation of shortwave hemispherical reflectance (albedo) from bidirectionally reflected radiance data," *Remote Sens. Environ.*, vol. 38, pp. 123–134, 1991.

[26] D. J. Diner, J. V. Martonchik, C. Borel, S. A. W. Gerstl, H. R. Gordon, Y. Knjazikhin, R. B. Myneni, B. Pinty, and M. M. Verstraete, *Level 2 Surface Retrieval Algorithm Theoretical Basis*, Jet Propul. Lab.,

Pasadena, CA, vol. JPL D-401, rev. C, 1997.
[27] M. M. Verstraete, B. Pinty, and R. E. Dickinson, "A physical model of the bidirectional reflectance of vegetation canopies 1. Theory," *J. Geophys. Res.*, vol. 95, no. D8, pp. 11 755–11 765, 1990.
[28] S. P. Ahmad and D. W. Deering, "A simple analytical function for bidirectional reflectance," *J. Geophys. Res.*, vol. 97, no. D17, pp. 18 867–18 886, 1992.
[29] G. Schluessel, R. E. Dickinson, J. L. Privette, W. J. Emery, and R. Kokaly, "Modeling the bidirectional reflectance distribution function of mixed finite plant canopies and soil," *J. Geophys. Res.*, vol. 99, pp. 10 577–10 600, 1994.
[30] H. Rahman, B. Pinty, and M. M. Verstraete, "Coupled surface-atmosphere reflectance (CSAR) model 2. Semiempirical surface model usable with NOAA Advanced Very High Resolution Radiometer data," *J. Geophys. Res.*, vol. 98, no. D11, pp. 20 791–20 801, 1993.
[31] R. B. Myneni, G. Asrar, and F. G. Hall, "A three dimensional radiative transfer method for optical remote sensing of vegetated land surfaces," *Remote Sens. Environ.*, vol. 41, pp. 105–121, 1992.
[32] R. B. Myneni and D. L. Williams, "On the relationship between FAPAR and NDVI," *Remote Sens. Environ.*, vol. 49, pp. 200–211, 1994.
[33] R. B. Myneni, F. G. Hall, P. J. Sellers, and A. L. Marshak, "The interpretation of spectral vegetation indices," *IEEE Trans. Geosci. Remote Sensing*, vol. 33, pp. 481–486, Mar. 1995.
[34] D. S. Kimes, "Dynamics of directional reflectance factor distributions for vegetation canopies," *Appl. Opt.*, vol. 22, no. 9, pp. 1364–1372, 1983.
[35] D. S. Kimes, W. W. Newcomb, R. F. Nelson, and J. B. Schutt, "Directional reflectance distributions of a hardwood and pine forest canopy," *IEEE Trans. Geosci. Remote Sensing*, vol. GE-24, pp. 281–293, Jan. 1985.
[36] D. S. Kimes, W. W. Newcomb, C. J. Tucker, I. Zonneveld, W. vanWijngaarden, J. deLeeuw, and G. Epema, "Directional reflectance factor distributions for cover types of Northern Africa in NOAA 7/8 AVHRR Bands 1 and 2," *Remote Sens. Environ.*, vol. 18, pp. 1–19, 1985.
[37] I. P. Grant and G. E. Hunt, "Solution of radiative transfer problems using the invariant S_n method," *Mon. Not. R. Astron. Soc.*, vol. 141, no. 1, pp. 27–41, 1968.
[38] M. I. Mishchenko and L. D. Travis, "Light scattering by polydisperse, rotationally symmetric nonspherical particles: Linear polarization," *J. Quant. Spectrosc. Radiat. Transf.*, vol. 51, no. 5, pp. 759–778, 1994.
[39] P. Koepke, "Effective reflectance of oceanic whitecaps," *Appl. Opt.*, vol. 23, pp. 1816–1824, 1984.
[40] H. R. Gordon, D. K. Clark, J. W. Brown, O. B. Brown, R. H. Evans, and W. W. Broenkow, "Phytoplankton pigment concentrations in the Middle Atlantic Bight: Comparison between ship determinations and coastal zone color scanner estimates," *Appl. Opt.*, vol. 22, pp. 20–36, 1983.
[41] J. E. Conel and S. Pilorz, *Science Data Validation Algorithm Theoretical Basis*, Jet Propul. Lab., Pasadena, CA, vol. JPL D-13403, 1997.
[42] J. E. Conel and W. C. Ledeboer, *Science Data Validation Plan*, Jet Propul. Lab., Pasadena, CA, vol. JPL D-12626, 1997.

John V. Martonchik, for a photograph and biography, see this issue, p. 1086.

David J. Diner, for a photograph and biography, see this issue, p. 1040.

Bernard Pinty, for a photograph and biography, see this issue, p. 1087.

Michel M. Verstraete (M'95), for a photograph and biography, see this issue, p. 1087.

Ranga B. Myneni, for a photograph and biography, see this issue, p. 1087.

Yuri Knyazikhin, for a biography, see this issue, p. 1249.

Howard R. Gordon, for a photograph and biography, see this issue, p. 1087.